A transmission electron microscopy and X-ray photoelectron spectroscopy study of annealing induced γ-phase nucleation, clustering, and interfacial dynamics in reactively sputtered amorphous alumina thin films

A. K. Nanda Kumar,[1,a)] S. Prasanna,[2] B. Subramanian,[1] S. Jayakumar,[3] and G. Mohan Rao[4]

[1]*ECMS Division, Central Electro Chemical Research Institute, Karaikudi, India*
[2]*Department of Physics, PSG College of Technology, Coimbatore, India*
[3]*Department of Physics, PSG Institute of Technology and Applied Research, Coimbatore, India*
[4]*Department of Instrumentation, Indian Institute of Science, Bangalore, India*

Pure α-Al$_2$O$_3$ exhibits a very high degree of thermodynamical stability among all metal oxides and forms an inert oxide scale in a range of structural alloys at high temperatures. We report that amorphous Al$_2$O$_3$ thin films sputter deposited over crystalline Si instead show a surprisingly active interface. On annealing, crystallization begins with nuclei of a phase closely resembling γ-Alumina forming almost randomly in an amorphous matrix, and with increasing frequency near the substrate/film interface. This nucleation is marked by the signature appearance of sharp (400) and (440) reflections and the formation of a diffuse diffraction *halo* with an outer maximal radius of ≈0.23 nm enveloping the direct beam. The microstructure then evolves by a cluster-coalescence growth mechanism suggestive of swift nucleation and sluggish diffusional kinetics, while locally the Al ions redistribute slowly from chemisorbed and tetrahedral sites to higher anion coordinated sites. Chemical state plots constructed from XPS data and simple calculations of the diffraction patterns from hypothetically distorted lattices suggest that the true origins of the diffuse diffraction halo are probably related to a complex change in the electronic structure spurred by the *a*-γ transformation rather than pure structural disorder. Concurrent to crystallization within the film, a substantially thick interfacial reaction zone also builds up at the film/substrate interface with the excess Al acting as a cationic source. © 2015 AIP Publishing LLC. [http://dx.doi.org/10.1063/1.4916331]

I. INTRODUCTION

The stable high temperature form of aluminium oxide α-Al$_2$O$_3$, also recognized by its commercial epithet of *corundum* or *kurundam* is a well-known ceramic, crystallizing in a rhombohedral structure (space group $R\bar{3}c$) with trigonal symmetry. Its inherent thermodynamic stability lends itself to the formation of a protective oxide scale in a range of Al-containing Fe- (FeAl, FeCrAl) and Ni- (NiCrAl, NiCrAlY, CoNiCrAlY) based high temperature structural alloys. Despite its high temperature stability, α-Al$_2$O$_3$ has a host of transient near-polymorphic low temperature predecessors— β, γ, η, κ, δ, χ and θ-Al$_2$O$_3$—in addition to some recently reported new phases: α′, λ, etc.[1,2] The tendency for hydrogen absorption into the lattice (hydrated aluminas) often leads to ambiguity on the exact polymorphic nature of the cubic transition aluminas, with claims that the hydrogen in the cationic sub-lattice leads to a tetragonal distortion.[3] On the other hand, some of the inter-transitory phase transformations— for instance the γ → η/δ transition—are also topotactic in nature (accompanied by just a rearrangement of the cations between the interstitial sites while the anionic framework is largely unaffected), while some others are reversible (the θ → α transition) leading to some unique twinning related habit planes between the parent and product phases. The

myriad number of transitory phases notwithstanding, the roles of both α and its predecessor phases as ceramics and catalysts are overwhelming, although our current understanding of the formation and growth kinetics and other microstructural aspects of the intermediate phases are limited.

Among the transition aluminas, γ-Al$_2$O$_3$ (which is the most common metastable phase) undoubtedly finds its greatest commercial relevance as a catalyst or as catalytic supports for other noble metals or mixed (Cr, Co) oxides used for the reduction of pollutants such as CO, nitrous oxides, and hydrocarbons in the exhaust manifold of automobiles.[4,5] The superior catalytic activity of γ-Al$_2$O$_3$ evolves from its large surface area (increased stability at specific surface areas exceeding 125 m^2/g, thereby capable of high porosity),[6] a low surface energy (≈1.5 J/m^2 as against ≈2.5 J/m^2 for α)[6] and the tendency to attract hydroxyl groups to its anion terminated surface.[7] Despite its metastability, γ is often observed to be the preferred initial phase to nucleate in thin aluminium oxide films grown for microelectronic applications such as gate oxides or high k dielectrics by both chemical[8] and physical vapour deposition routes.[9] Interestingly, it is also (along with κ), the first phase to nucleate during initial state oxidation of high temperature aluminides, such as NiAl.[10] However, surface oxidation and film deposition are fundamentally different processes: the former involves equilibrium reaction kinetics while the latter most often produces a disordered amorphous state without

---

a)Author to whom correspondence should be addressed. Electronic mail: aknk27@yahoo.com

117, 125307-1

undergoing a glass transition. Yet, in both cases, the transient γ once formed persists even at temperatures as high as 1200 °C.[11] Of late, purely amorphous Al_2O_3 (a-Al_2O_3) films obtained by sputtering and electron beam evaporation have also been investigated as promising ultrathin dielectrics with a dielectric constant, ε ($\varepsilon_{lattice} + \varepsilon_{electronic}$) comparable to α-Al_2O_3 (roughly between 8 and 11).[12] Such pristine a-Al_2O_3 coatings also exhibit a very low leakage current density of $\approx 10^{-3}$ A/cm^2 at 8 MV/cm, which is significant compared to γ-Al_2O_3 (which showed the same leakage current density at 2.5 MV/cm).[13] Hence with the increasing technological impact of both γ and a-Al_2O_3, understanding the fundamental nature of their transition assumes significance.

Analysis of various reports reveals that a-alumina is quite unstable against crystallization, but γ-alumina presents a high degree of metastability before transforming to α. Assorted evidences point to a mechanism whereby the propensity of a-Al_2O_3 to crystallize to γ-Al_2O_3 occurs through atomic shuffling and short range re-ordering effects that are associated with activation energies of the order of 4–6 eV.[14,15] This hypothesis is also borne out by reports that the diffusivity of the rate controlling oxygen species in a-alumina is almost *2–3 orders of magnitude higher* than in γ-alumina with a low activation energy of 1.2 eV.[16] The large free volume of the amorphous structure enables easy diffusional pathways for crystallization, but the thermodynamic stability offered by the transition aluminas (particularly γ) at low length scales freezes the system into an intermediate state with a surprisingly long life time. The intrinsically high metastability of the γ phase coupled with a high surface area makes it an intriguing polymorph of α-Al_2O_3. Another interesting aspect of such amorphous thin films is that the film/substrate interface is also surprisingly active. The inhomogeneity is often manifested as a metal ion enrichment at the interface or as a thick interfacial reaction zone (IRZ) that develops with annealing. Reports on IRZ formation in magnetron sputtered Al_2O_3 thin films have been reported, although there is a considerable variation in the reported thickness of the IRZ (between 10 nm to more than 100 nm).[17,18] Similar observations of cation enrichment in the initial layers of related catalytic support systems like RuO_2 (Ref. 19) and NiO[20] even at high oxygen pressures (in excess of 1 mbar) have been reported and mechanisms based on critical nuclei size for oxygen incorporation into the metal and the stability of the metal clusters against oxide clusters have been proposed. This paper expands on pre-existing records on transformations in amorphous alumina thin films, deposited by an energetic plasma sputtering technique and provides direct evidence of IRZ formation and microstructural evolution on annealing.

II. EXPERIMENTS

Thin films of aluminium oxide were reactively deposited in an O_2+Ar atmosphere from a pure (99.99%) Al target using direct current magnetron sputtering. We relied on X-ray photoelectron spectroscopy (XPS) to estimate O/Al ratios for a range of oxygen flow rates and partial pressures. After optimization, good reproducible coatings of reasonable thickness could be obtained at 0.001 mbar Ar and 0.0003 mbar O_2 partial pressures and a total sputtering power of

70 W (all films were slightly Al rich). Depositions were carried out on Si (100) wafers that were ultrasonically cleaned and HF etched just before loading into the deposition chamber. The target was initially pre-sputtered for 10–20 min until a steady voltage was ensured. After deposition, the samples were annealed in vacuum ($\sim 10^{-5}$ mbar) for 1 hour at 350 °C, 550 °C, and 750 °C.

A. XPS analysis

A SPECS GmbH X-ray photoelectron spectrometer (Phoibos 100 MCD Energy Analyser) using Al K$_\alpha$ (1486.6 eV) was employed for the XPS analysis. A sputter gun inside the chamber was used to clean the sample surface prior to analysis. Survey spectra of the films were recorded at a constant pass energy of 22 eV and the high resolution spectra were recorded with 25 eV pass energy. To avoid ambiguity of Ar incorporation into the films during sputter cleaning, two survey spectra—one before and another after sputter cleaning—were acquired and compared. The Ar photo electron signals at ≈ 240 eV in the BE scale were observed only in the sputter cleaned sample, thereby obviating the possibility of Ar incorporation into the films during deposition. The absence of Ar in the interior of the film was also confirmed by X-ray energy dispersive spectroscopy (XEDS) in the conventional TEM (C-TEM) mode. In the initial runs, it was observed that a significant amount of charge built up during photon irradiation in the films (as seen from a substantial shift of the Carbon peak by more than 4 eV, and interestingly this effect was very prominent in the annealed films). Therefore, a conductive layer of Au was deposited on all the films and calibration was done by placing the Au $4f_{7/2}$ line at 83.8 eV.

B. Specimen preparation for TEM

Specimens for TEM analyses were prepared by focused ion beam (FIB) machining of the thin film samples. Ga ions were used for milling and low energies were used to ensure that beam induced damage and curtaining effects were minimal. A JEOL–2010 F instrument equipped with a 200 kV FEG source and XEDS, Scanning TEM (S-TEM) capabilities was used for analysis. All images were recorded in conventional TEM mode and the dark field (DF) images were used to calculate crystallite size. S-TEM mapping was used to confirm the compositional inhomogeneity at the film-substrate interface. As reported in Sec. III B, the films were mostly amorphous and diffraction contrast was rather faint due to a strong background arising from the amorphous matrix that almost masked the diffraction signal. Since no energy filters were used, to clarify the features for crystallite size measurement, the recorded micrographs were first converted to 8 bit gray scale images and for each image, a background was determined using an erode-dilate algorithm,[21] which uses a disc shaped selection area of controlled radius and assigns a pixel value to the origin of the disc based on the pixel value at its neighbourhood. This background level was then subtracted from the DF image leading to clearer features in a uniformly dark background. After generating a uniform gray scale image, the gray level histogram was used
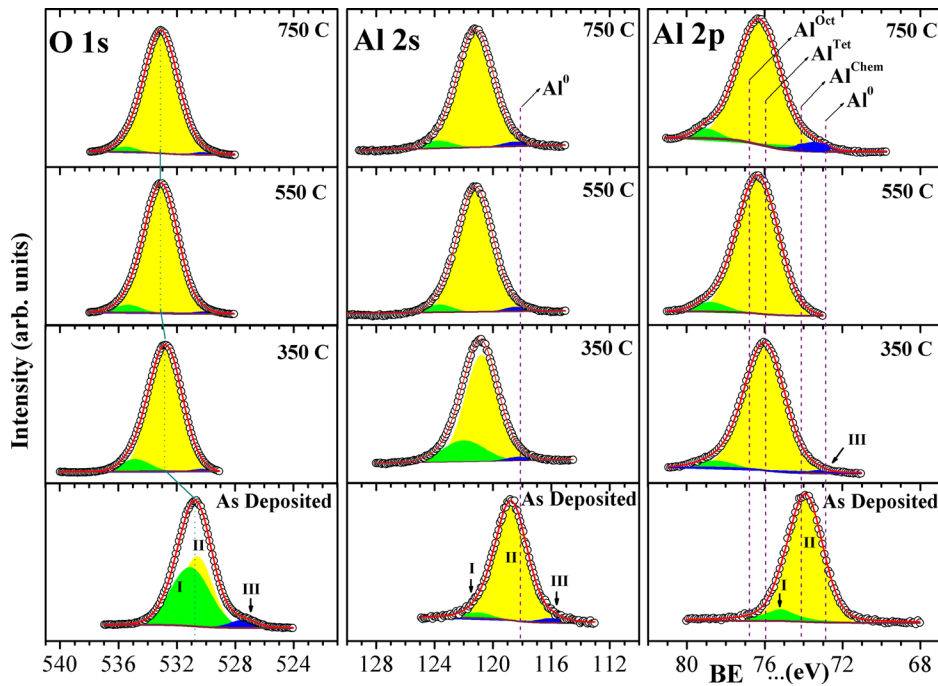
FIG. 1. Deconvoluted XPS peaks of O1s, Al 2s, and Al 2p of the as deposited and annealed films.

to select the contrast level for creating a mask. In all cases, the histogram was nearly Gaussian; 95% of the total intensity profile was selected from the histograms (so as to exclude the tail region of the histograms) and a mask was created. Applying this mask to the gray scale image filtered out all the background outside of the 95% intensity limit, rendering a binary black-white image. This image was used for quantification of the grain size data. Clustering was resolved by segmenting the larger grains in the binary image either automatically or manually by comparing with the gray scale image, so that it agreed with the original feature discernible in the micrograph. Measured diameters refer to the average length of lines drawn across the white regions (in a DF processed image) at 2° intervals. Too large clusters or very small grains (amounting to a few pixels) were precluded from further analysis to avoid ambiguity. Using the above mentioned procedure, more than 100 grains (domains contributing to the diffraction pattern (DP)) could be easily sampled from different micrographs in each specimen and the data reported herein were obtained after statistically analysing approximately 100–200 such grains from each specimen. An attempt was also made to calculate the size of the diffracting domains from the width of the Debye rings in the electron diffraction pattern. After comparison, the average crystallite size calculated by segmenting the binary images and measurement of the line width of the diffraction rings did not yield any significant difference, and hence employment of the former method to calculate crystallite size was justified.

III. RESULTS

A. XPS analysis

Fig. 1 shows the high resolution scans of the Al 2p, Al 2s, and O 1s photo electron peaks. All the annealed films showed a clear positive shift of the binding energies (BEs)—

TABLE I. Parameters obtained from deconvolution of XPS data, arranged in descending order of deconvoluted peak areas. Values in brackets indicate FWHM.

Sample	Al 2p (Γ) eV	O 1s (Γ) eV	Al 2s (Γ) eV	ΔBE eV	α' ($=BE+KE$) eV
As deposited	73.89 (2.08)	531.08 (3.18)	118.79 (2.27)	457.2	1038.15
	75.2 (1.92)	530.61 (2.42)	121.03 (3.93)		
		527.49 (2.12)			
350 °C	76.0 (2.5)	532.75 (2.67)	120.78 (2.72)	456.75	1039.35
	78.52 (2.09)	534.84 (2.35)	122.02 (3.4)		
	73.31 (1.06)	530.33 (1.15)	118.25 (1.92)		
550 °C	76.36 (2.48)	533.09 (2.74)	121.22 (2.83)	456.73	1039.2
	78.8 (1.93)	535.34 (2.10)	123.66 (2.07)		
		530.13 (1.38)	118.41 (1.9)		
750 °C	76.28 (2.66)	533.1 (2.81)	121.22 (2.90)	456.82	1038.2
	78.99 (1.5)	535.53 (1.77)	123.81 (2.41)		
	73.46 (1.71)	530.27 (1.44)	118.5 (2.14)		

although in varying degrees—from the as deposited film. After a Shirley background subtraction, non-symmetric peaks were deconvoluted using a combined Gaussian and Lorentzian (a Pseudo Voigt) function and a Levenberg-Marquardt minimization algorithm into their sub components. For brevity, the deconvoluted photo electron spectral parameters are presented in Table I. In principle, it is possible to distinguish tetrahedral (Al^{Tet}) and octahedral (Al^{Oct}) aluminium in Al_2O_3 from the more positive BE shifts of Al^{Oct} owing to the higher net electronic charge residing on the Al ion in the $[AlO_6]^{9-}$ octahedron than in the $[AlO_4]^{5-}$ tetrahedron. Aluminium in α or γ alumina can also be distinguished from a comparison of the FWHM (Γ) of the Al 2p peaks ($\Gamma \approx 2.5$ in γ and 1.35 in α). The Al 2p spectrum of the as deposited film was deconvoluted into two peaks centred at 73.89 eV and 75.2 eV. We found two close corroborations from pertinent systems: one reported by Bicker *et al.*[22] and another recent one by Mulligan *et al.*,[23] which were carried out on alumina doped silicates and nanometre thick oxide scales on NiAl, respectively. Mulligan *et al.*[23] report the observation of Al^{Tet}, Al^{Oct} and a third peak arising from chemisorbed oxygen on aluminium (Al^{Chem}). The Al^{Chem} species is associated with aluminium coordinated to less than 4 chemisorbed oxygen atoms on the surface.[24] In Fig. 1, the positions of metallic (Al^0), Al^{Chem}, Al^{Tet}, and Al^{Oct} (taken primarily from Refs. 22, 23, and 25, and standard XPS databases) are marked for comparison. Remarkably, it appears to be a low BE (chemisorbed) aluminum species that is dominant in the as sputtered film ($\sim$90%). A second minor peak that can be ascribed to Al^{Tet} was also observed with a relative fraction of 10%. In the 350 °C annealed specimen, tetrahedral Al shows up predominantly ($\sim$98%). However, a minor fraction of metallic Al signal could also be distinguished. The tail at higher BE also showed a peak that was present in all the annealed specimens. The BE shift for this peak was too large to attribute it to a pure oxide phase and must probably arise from hydroxide formation on the surface during annealing or by differential charging. With increasing annealing temperature, the major peak stabilizes somewhere between Al^{Tet} and Al^{Oct} positions indicating a mixed co-ordination between 4 and 6 anions. Interestingly, the 750 °C specimen also showed a small fraction of metallic Al ($\sim$4%) in comparison with the other specimens, suggesting that on increasing the annealing temperature, the microstructure becomes Al-rich on the surface, either by oxygen desorption on the surface or by Al diffusion from the interface to the surface through the open porous microstructure of the amorphous film. The Γ of the major deconvoluted Al 2p peak in all the annealed specimens lay between 2.4 and 2.6 eV, in agreement with that reported in literature for Al in γ-Al_2O_3. The Al 2s peak was also deconvoluted into three sub peaks. The net effect of annealing was to shift the peaks to higher BEs. The major peak in the as deposited film was observed at 118.79 eV which on annealing increased progressively to 121.2 eV. Interestingly, the low BE tail showed metallic Al in all annealed specimens, indicating a microstructural inhomogeneity in the films. The Γ of O 1s can also be used to identify oxygen in α (1.58 eV) or γ (2.8 eV). The major resolved component in all the annealed specimens had Γ between 2.4 and

2.8 eV. On average, there was a shift of roughly +2 eV of all the peaks on annealing. However, in the as-deposited sample, two close peaks, the largest of which can be ascribed to a hydroxide compound[26] most likely from moisture absorption during deposition could be distinguished.

In a series of reports by Yoshitake *et al.*,[27–29] distinct BE shifts of both Al and O in pristine and *in-situ* oxidized Al-containing alloy surfaces were observed. Using varying photon energies and different take-off angles, they demarcated the Al species in the oxide scale, the scale/alloy interface, alloy surface and bulk alloy, attributing the shifts not to local chemical co-ordination, but to a change in the band alignment originating from the nature of the layer at the scale/substrate interface (epitaxial/amorphous and Al/O terminating species). However, the oxide scales in their study were less than 2 nm thick and the band bending was validated using VB edge studies. Although this possibility can be partly ruled out due to the Au-capped layer in the present case, the large thickness of our films ($>$500 nm) precluded a more detailed study of the band alignment at the interface. To avoid the ambiguity of peak assignment based on absolute values of BE alone (arising from differential charging and energy scale calibration offsets), the BE difference between the strongest Al 2p and O1s peaks (ΔBE) were calculated. As can be seen from Table I, ΔBE in the pristine film was 457.2 eV, while for all the annealed specimens ΔBE was consistently at 456.7–456.8 eV. These values are in accordance with other reports of γ-Al_2O_3 (456.9 eV, 457.2 eV),[30,31] a-Al_2O_3 (456.8 eV),[28] epitaxial Al_2O_3 on NiAl,[29] and atomic layer deposited (ALD) Al_2O_3 films (456.6 $\pm$ 0.1 eV).[32] While all these values attest to the formation of the oxide, the shift in ΔBE of $\sim$0.5 eV indicates a change in the bonding nature of the films on annealing. A purely ionic Al_2O_3 is expected to have a larger separation (ΔBE) than a mixed covalent oxide.[33] In reality, Al_2O_3 is a partially covalent oxide ($\sim$50% covalent on the Pauling scale). The O 1s is also closer to Al 2p in the annealed than in the as deposited films, implying that the oxidic nature improves with annealing, in comparison to the pristine films. While the increase in the BE values of both Al and O confirms Al-O compound formation in the sample, substantial shift from standard values also indicates that the oxidation states have been strongly altered. The significantly large fraction of tetrahedrally coordinated Al is a direct indication of the fraction of amorphous alumina in the films, since the only phase with a high Al^{Tet} is a-Al_2O_3.

B. TEM analysis

A preliminary look of the annealed specimens indicated island-like growth of the Al-rich layer near the interface at 350 °C; however, at 550 °C, the film/substrate region abruptly developed an $\sim$150 nm thick IRZ, which evolved little with further annealing to 750 °C (Figs. 2(a)–2(c)). Both diffraction and XEDS analyses were carried out in the C-TEM mode, whereas line scans were obtained in the scanning mode. Some of the primary reflections of Si and γ-Al_2O_3 match closely, and hence the true film reflections for dark field imaging were obtained from an area roughly 300–400 nm away from the interface. The chemical
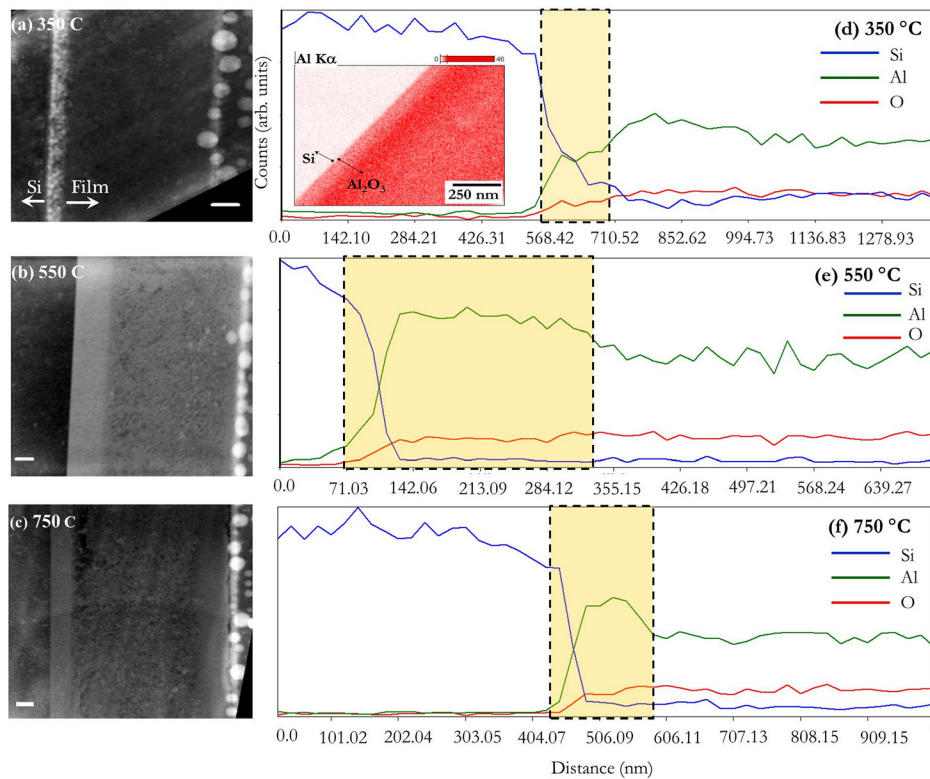
FIG. 2. Cross-sectional TEM bright field images and concentration profiles along a line scanned across the interface of annealed Al_2O_3/Si films: (a), (d) 350 °C; (b), (e) 550 °C; (c), (f) 750 °C. In (a)–(c), all distance markers represent 100 nm. The inset in (d) is a S-TEM composition map around the interface of the 350 °C annealed sample constructed using the Al Kα line.

composition of the IRZ was checked by XEDS point analysis in the C-TEM mode with a probe size of 1 nm. Spectra were quantified using the K_α lines of Si, Al, and O and applying the Cliff-Lorimer correction procedure. A minimum of four different points within the IRZ were analysed for composition and the average values are reported. It is worth mentioning that the observation of the as-sputtered film by cross-sectional FE-SEM only showed a thin layer of SiO_2 on the substrate surface (figure not shown), implying that the IRZ developed only on annealing. The following paragraphs describe the C-TEM observations on the annealed specimens. The results are also briefly summarized in Table II.

In the film annealed at 350 °C, towards the substrate side of the IRZ, recrystallization of Si was obvious by the occurrence of the (111), (220), and (311) reflections corresponding to measured d_{hkl} of 0.314 nm, 0.192 nm, and 0.164 nm, respectively (Figs. 3(a) and 3(b)). At higher magnifications, the thin native oxide (of Si) was always observed on the surface of the substrate. Even after tilting the sample, no diffraction could be observed from the IRZ which is apparently amorphous.

Interestingly, the IRZ was not only Al-rich but also had a high concentration of Si in comparison to the other specimens (ref. Table II). Moreover, the Si enrichment was not restricted only to the IRZ, but was fairly high throughout the film, indicating that the open structure provided by the amorphous film may have aided Si diffusion. The Al-Si phase diagram shows a higher solubility of Si in Al and hence, the Si enrichment near the interface probably occurs by the substrate diffusing into the amorphous Al-rich film very near the interface. A line analysis in the S-TEM mode showed evidence of compound formation by Si diffusion (a flattening of the Al and Si concentration profile) followed by the Al-enriched region (Fig. 2(d)). On the film side of the IRZ (Figs. 3(c)–3(e)), two intense reflections, corresponding to the (400) and the (440) reflections from the transient γ alumina phase were evident. Interestingly, a well-defined disc was observed in the DP from the origin of the reciprocal lattice (RL) space to a distance of $d_{max} = 0.233$ nm. The diffraction ring from the $d_{hkl} = 0.314$ nm plane attributed to Si (111) is also visible within the disc. On moving further away from the IRZ towards the film (∼300 nm from the IRZ),

TABLE II. Summary of observations from the cross-sectional TEM analyses (of the diffraction patterns and XEDS point analysis in C-TEM mode) of the annealed foils.

| Specimen	Composition of IRZ (at. %)			Strongest reflections in the film, d_{hkl} in nm/(hkl)	d_{max} of the diffuse halo (nm)		Average crystallite size (nm)
	Al	O	Si		IRZ	Film	
350 °C annealed	48.88 ± 0.84	37.42 ± 1.49	13.69 ± 2.24	0.139 /(400)$_\gamma$ 0.192 /(440)$_\gamma$	0.237	0.233	5.25 ± 0.22 (sd: 2.55)
550 °C annealed	70.46 ± 1.71	25.97 ± 1.27	3.56 ± 0.79	0.132 /(400)$_\gamma$ 0.192 /(440)$_\gamma$	0.227	0.227	6.69 ± 0.35 (sd: 4.75)
750 °C annealed	52.71 ± 6.44	41.14 ± 5.36	6.14 ± 1.96	0.131/ (400)$_\gamma$ 0.191/ (440)$_\gamma$	0.227	0.227	7.83 ± 0.27 (sd: 3.76)
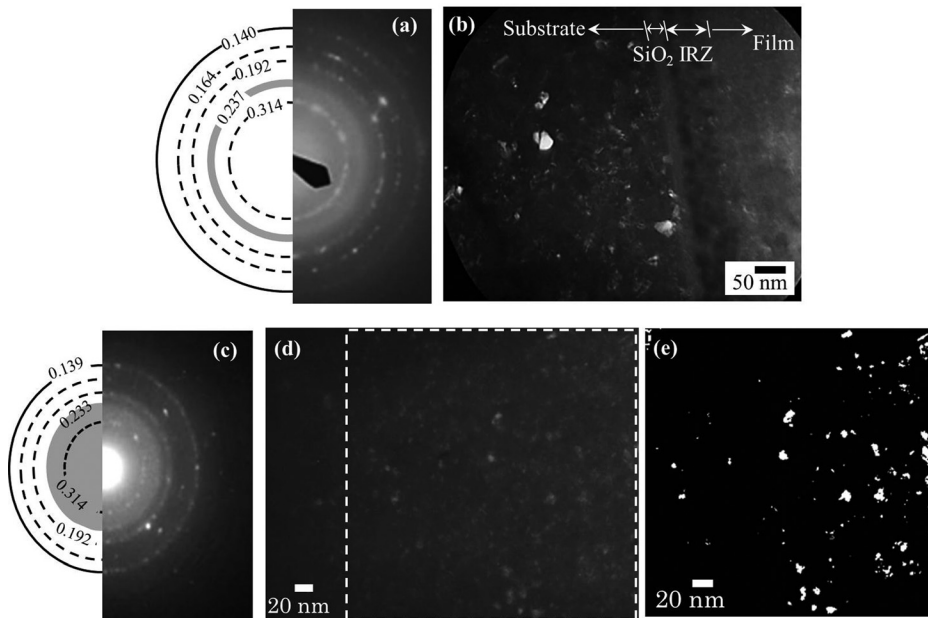
FIG. 3. (a) DP and (b) DF image of substrate side of the interface in the 350 °C annealed film. The DF was recorded using the continuous ring marked in the DP; (c) DP from the film side of IRZ in the 350 °C film; (d) corresponding gray scale DF image from the ring marked with a continuous line in (c); (e) unsegmented, processed binary image (slightly enlarged) of the region marked by the box in the DF in (d).

this innermost ring disappeared completely, and all reflections of the γ phase showed up, including the (111) planes spaced at 0.443 nm (comparison with the actual value from ICDD 29–1486 shows a slight reduction by almost 0.013 nm). When diffraction experiments were attempted at the film/air interface, no diffraction could be observed. Evidently, crystallization starts at the substrate/film interface and seems to propagate from the interface towards the surface. Crystal nuclei sizes calculated by the procedure described earlier showed an average diameter of 5.25 ± 0.22 nm (sd: 2.55), as shown in Fig. 4 and Table II.

In the film annealed at 550 °C, the DPs recorded from the substrate side of the IRZ were clearly attributed to the substrate (Fig. 5(a)), similar to the 350 °C specimen. Interestingly, when a DF image was obtained from the $d = 0.196$ nm ring, diffraction contrast was observed from *within the IRZ* (Figs. 5(b) and 5(c)). Careful analysis of the DP by measuring the gray level histograms showed two closely spaced rings (a second one at 0.207 nm). Unlike the 350 °C annealed sample, in which the IRZ was practically
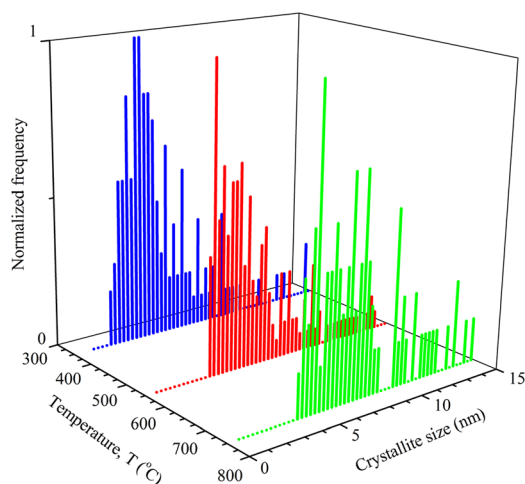
devoid of any diffraction contrast, spherical nuclei-like features were observed in the thick IRZ in this sample, along with small recrystallized grains in the Si substrate. Such crystallization in Al-rich microstructures has been reported previously.[34,35] The Debye ring of 0.207 nm arises from incipient Al-rich Al-O clusters due to the high cationic segregation in the IRZ. Accordingly, the XEDS analysis at the IRZ showed extensive Al-enrichment ($\sim$70 at. %, ref. Table II) in agreement with the notion of oxygen dissolved Al cluster formation. Since the specimen was slightly thick and non-uniform at the interface, we did not attempt lattice fringe imaging of these clusters. The line profile in S-TEM mode also showed uniform Al-enrichment over the entire IRZ (Fig. 2(e)), devoid of any step in the concentration profile of either Si or Al, and also a significant reduction of the Si content in the film compared to the 350 °C annealed specimen. The prominent reflections in the film were again $(440)_\gamma$ and $(400)_\gamma$ as seen in Figs. 5(d) and 5(e). The diffuse halo was also present at a d_{max} of $\approx$0.227 nm (which incidentally is close to $(222)_\gamma$).

The film annealed at 750 °C showed enhanced nucleation in the film. Diffraction from the substrate side of the IRZ showed reflections from the Si substrate. From the film side of the IRZ, in addition to the two primary reflections from (440) and (400) γ, the diffuse halo with a d_{max} of 0.227 nm was clearly evident (Fig. 6). The DF images also showed nucleation of spherical grains in the IRZ, similar to those observed in the 550 °C sample. However, the frequency of these IRZ nuclei was rather sparse when compared to the former sample. During FIB machining of this sample, a thin crack appeared and propagated parallel to the IRZ/film junction (visible in Fig. 2(c) and also in Fig. 6(b)). Probably, a large intrinsic stress following a reduction in the free volume by densification showed up as an interfacial crack as the film was thinned. In some regions, this crack was observed to move towards the film surface leading to a pre-delamination scenario. In comparison, the IRZ/substrate interface showed excellent adhesion. Clearly, the diffusion

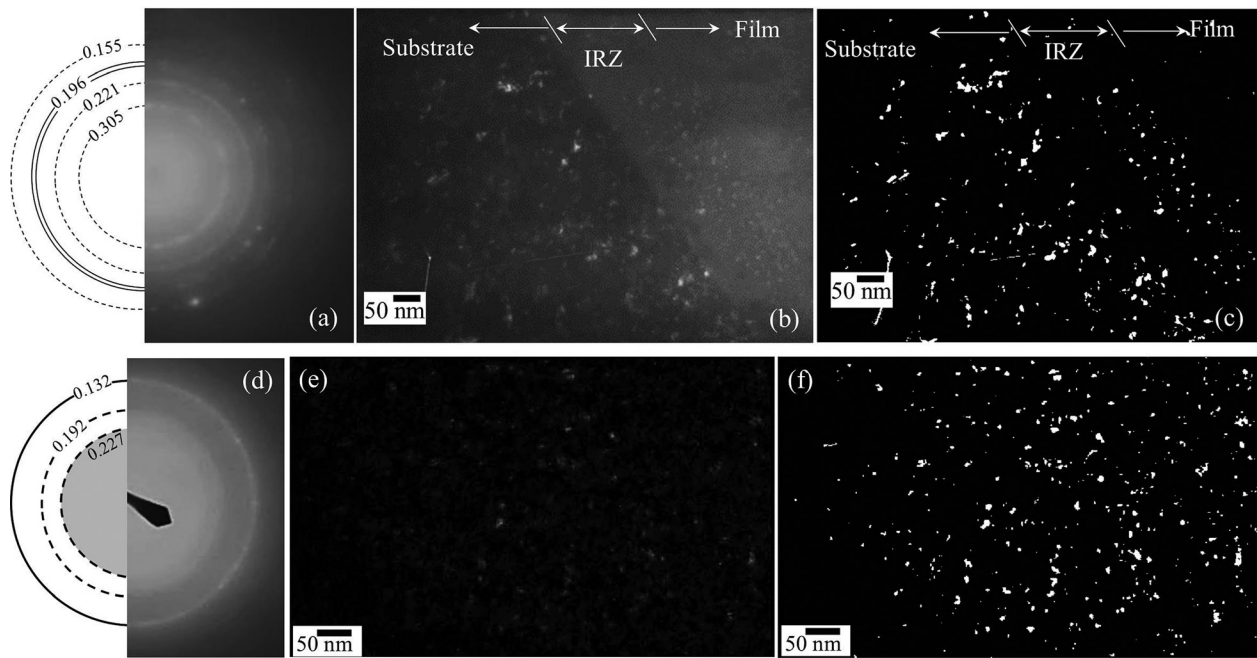FIG. 4. Crystallite size distribution in the annealed Al_2O_3 films.

FIG. 5. (a) DP from the substrate side of IRZ of the 550 °C annealed film; (b) corresponding gray scale DF image from the ring marked with a continuous line in (a); (c) processed (slightly enlarged) binary image of the region marked by a dashed box in the DF in (b); (d) DP from the 550 °C annealed film; (e) corresponding gray scale DF image from the ring marked with a continuous line in (d); (f) processed binary image of (e).

of Si at high temperatures into the IRZ has introduced a strong chemical mixing between the Al-rich film and the substrate forming a dense, amorphous silicate. In addition to the usual Al enrichment in the IRZ, the Si content was significantly less in comparison to the 350 °C sample (Fig. 2(f) and Table II). Further into the film, larger crystallites could be clearly discerned; however, they seemed to grow by a cluster coalescence mode rather than by normal diffusional growth across grain boundaries (Fig. 7), and the crystallite size increased marginally to 7.83 ± 0.27 nm. Even in the film region, along with the two primary reflections attributed to the γ phase, the amorphous disc was clearly evident with $d_{max} = 0.227$ nm.

These observations on the interfacial dynamics of the sputtered films are surprising, since while crystalline Al_2O_3 is thermodynamically stable over Si (ΔG is highly positive for the forward reaction $2Al_2O_3 + 3Si = 3SiO_2 + 4Al$), the interface for this a-Al_2O_3/Si thin film system is apparently very active. Hence, it can be anticipated that structural

factors (defect density and vacancy population, which can vary drastically with the method of deposition and plasma parameters) and the nature of the substrate surface (orientation and pre-existence of an oxide terminated surface layer) can play decisive roles in the formation and the growth kinetics of the IRZ. In Sec. IV, we discuss the probable origins of the unique observations, viz., the signature appearance of the (440) and (400) reflections, the diffuse halo and crystallization mechanism by clustering.

IV. DISCUSSION

γ-Al_2O_3 crystallizes in an almost cubic spinel structure (the c/a is not exactly unity, but slightly stunted by almost 2%) like $MgAl_2O_4$, except that the divalent Mg^{2+} ion is replaced by the trivalent Al^{3+} cation and the occupancy of the interstitial voids (V_{Al}''') is such as to balance the total anionic charge (Fig. 8). In crystallographic descriptions of the γ phase as a defective spinel, the distribution of the Al
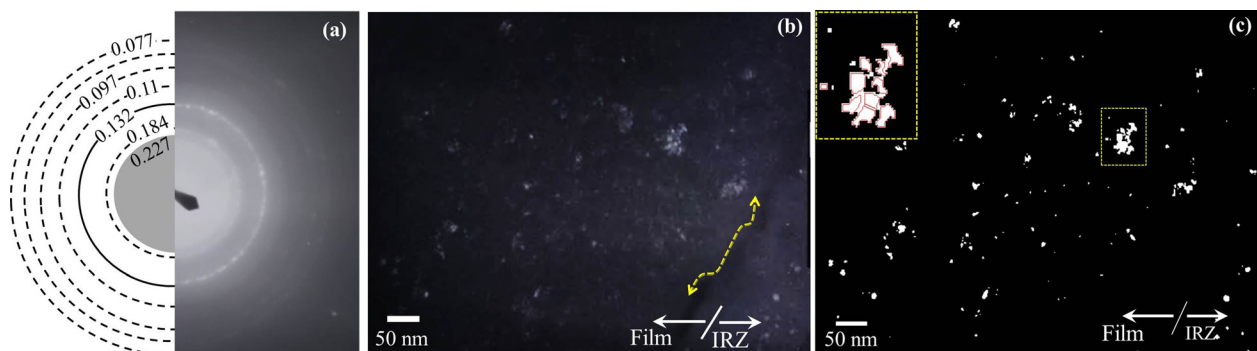

FIG. 6. (a) DP from the film/IRZ region of the 750 °C annealed specimen; (b) corresponding gray scale DF image from the ring marked with a continuous line in (a)—the dotted arrow shows an interfacial crack that propagates at the film/IRZ junction and parallel to the IRZ; spherical crystallites can also be discerned in the IRZ; (c) processed binary image of (b); the inset in (c) shows a cluster that was segmented to show a number of crystallites.
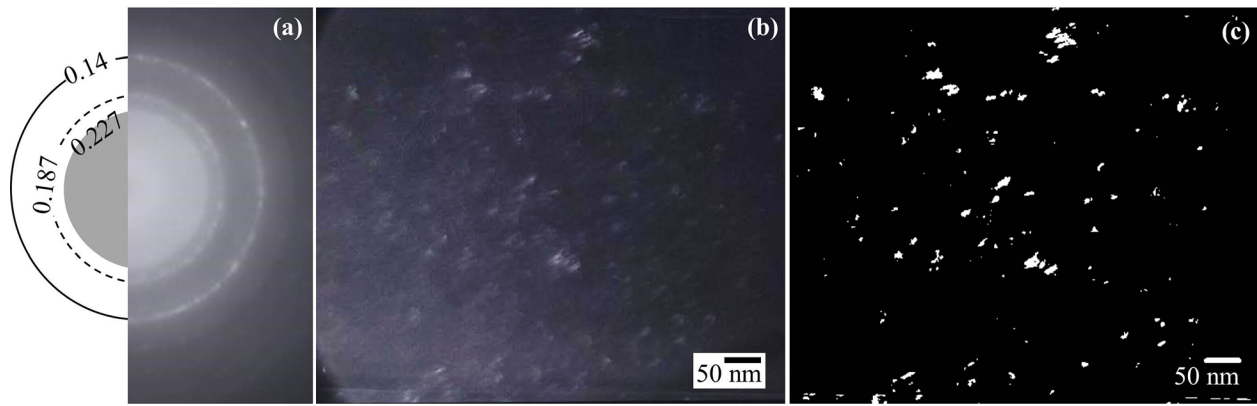
FIG. 7. (a) DP from the film annealed at 750 °C; (b) corresponding gray scale DF image from the ring marked with a continuous line in (a); (c) processed binary image of (b).

cations between the tetrahedral (the 16d Wykoff sites) and octahedral sites (the 8a Wykoff sites) has been addressed, although seemingly unresolved.[36,37] While the Al cation is expected to achieve its ground state by octahedral co-ordination, various results seem to suggest otherwise. For instance, Zhou and Snyder[38] after conducting a detailed X-ray and neutron powder diffraction investigation on both the η and γ phases suggested that the cation voids are distributed *randomly* in the tetrahedral and octahedral sites. On the other hand, theoretical investigations using *ab initio* density functional calculations suggest that the minimum energy configuration of the γ lattice is the one for which all the 8/3 cationic vacancies are located only in the octahedral sites.[39] This disparity in the ordering of the Al sub-lattice notwithstanding, what most reports agree upon is that the ordering of the anion (O) sub-lattice is almost perfect (in a face-centred close packed *ABC*-type stacking).

From the present work, it is obvious that the sputtered alumina films tend to crystallize by coalescing in the γ phase before transforming to the more stable α. The current understanding among the scientific community is that the ordering of the anion sub-lattice during the a-γ transition occurs faster than the cation ordering. This notion is validated by experimental observations: reflections arising from predominantly O–dominated planes like the (222), (400), and (440) tend to
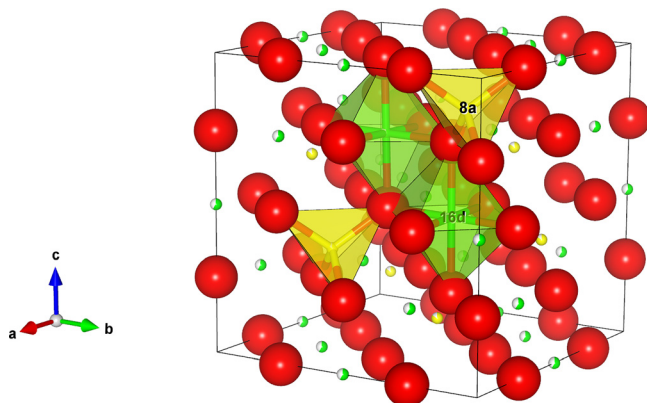
be sharp and strong in XRD patterns. This fact undoubtedly has some bearing on the consistent observation of the intense (400) and (440) reflections in our samples. However, unlike X-ray scattering which occurs by the electron cloud surrounding the atom, the atom form factors for electron scattering, f_{el}—which correspond directly with the scattered wave intensity in the TEM experiments—are dependent on the Coulomb field of the *nucleus* of the scattering atoms. Hence, the electron diffraction patterns would be affected to a greater extent by the larger oxygen sub-lattice (ordering or disordering) than by the smaller cationic Al sub-lattice, since f_{el} increases with atomic size at low scattering angles, which is the case in electron diffraction. The absence of a sharp (222) reflection and instead, the appearance of a diffraction halo with a $d_{max} \approx 0.227$ nm ($\cong d_{222}$ of γ) in the present case must therefore be correlated in some way to a transition of the anions (since they populate the (222) planes) from random sites to more definite positions in the oxygen sub-lattice of the nucleating γ phase. However, the diffuse Debye halo cannot arise from a merely random lattice shuffle. To confirm this, we conducted a simple calculation of the diffraction pattern as a function of the lattice distortion by considering the projection of the ideal γ lattice along [440]. Each atom on the projected plane was modelled as a Gaussian point spread function (*psd*) whose intensity scales as its atomic scattering factor, f_{el}. Since this is a 2D projected lattice, the interaction of the incident electron beam with this *psd* will effectively produce the diffraction pattern contained in the zeroth order Laue zone (ZOLZ). 150 oxygen anions at the 32e sites and 100 Al cations (for charge neutrality) at the 8a and 16d sites were used in the model lattice. The total Al vacancies were then partitioned equally between the tetrahedral and octahedral sites, randomly. The diffraction pattern was then simulated using a Fourier transform algorithm (Figs. 9(c) and 9(d)). The ionic positions in the ideal lattice were next slightly and randomly distorted (we tried three realistic magnitudes of distortion: ±5%, ±10%, and ±15% of the lattice spacing) and the DP was simulated to see how the diffraction pattern is affected by the disorder in the lattice. As seen from Figs. 9(e) and 9(f), in comparison with the diffraction pattern of the undistorted lattice, there was no significant change in the *positions* of the calculated diffraction
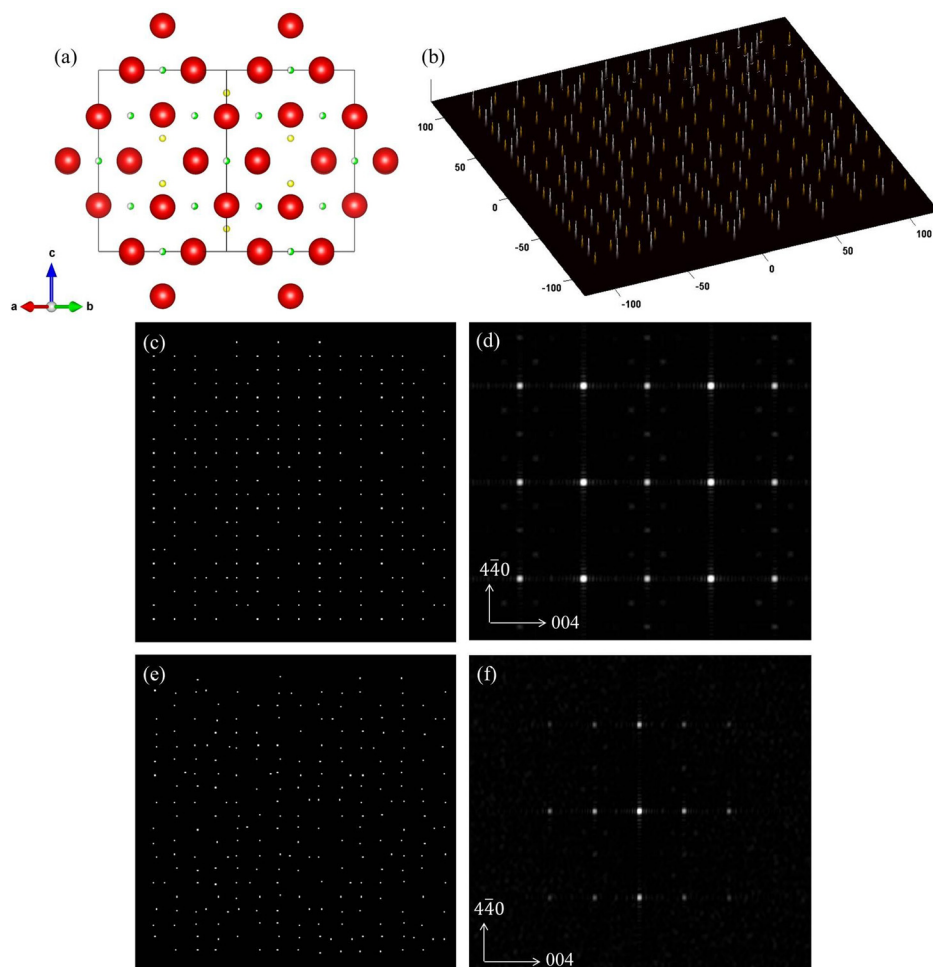

FIG. 8. Structure of γ-Al$_2$O$_3$ with the 8a (yellow) and 16d (green balls) Wykoff sites marked to distinguish tetrahedrally and octahedrally co-ordinated cations. Co-ordinates taken from Zhou and Snyder.[31]

FIG. 9. (a) [440] projection of γ-Al_2O_3 structure; (b) A 3D plot of the psd used to simulate the undistorted lattice; (c) 2D projection of the psd of the undistorted lattice shown in (b) along [440]; (d) simulated DP of the undistorted lattice in (c), the slight streaking of the reflections is due to the Fourier synthesis; (e) 2D projection of the psd of a lattice along [440] with all atoms distorted $\sim$15% from their mean positions; (f) simulated DP of the 15% distorted lattice (the background is observed as random faint dots surrounding the main reflections).

pattern, but the *background intensity increased* with the shuffle magnitude. No additional spots were detected in the calculated ZOLZ pattern. This simple analysis can be extended to polycrystalline specimens too, where the Laue cone is produced by all possible rotations of each diffracting plane along the zone axis. Hence, the diffuse halo extending to precisely 0.227 nm observed in our experimental diffraction pattern is not an effect of a simple shuffle of atomic positions, but has a rather more complex electronic basis involving atomic vacancies and charge distribution that affects the scattering factor of the atoms involved in the diffraction. This is supported by the XPS studies also, as we discuss later.

Interestingly, the occurrence of a diffuse diffraction halo seems to be a characteristic trait observed only in γ-alumina. While Bai *et al.*[40] have observed it in mesoporous alumina, Engelhart *et al.*[41] have reported a similar but detailed observation in dual magnetron sputtered Al_2O_3 thin films. Using energy filtered TEM, they[41] interpreted that the extent of spread of the diffuse disc was dependent on the degree of disorder in both the Al and O sub-lattice. Moreover, it was concluded that the disorder might be stabilized by inclusion of Ar ions (introduced by the sputtering gas). The structure factors are altered by the presence of Ar in the Al sub-lattice, leading to what they term a "pseudo-γ" phase. However, the article does not report the O/Al concentration. In the present

studies, we did not find the presence of Ar by XEDS or XPS. Instead, the O/Al ratio indicated an Al-rich composition (at 350 °C the ratio was 1.2 which increased to nearly 1.38 at 750 °C on annealing) and similar diffraction halos in DPs were observed. Hence, incorporation of Ar in the Al sublattice may not be the sole cause for the appearance of a diffraction disc. Instead, it is possible that disorder introduced by an anion (oxygen) deficient sub-lattice ($V_O^{\bullet\bullet}$) or a cation excess lattice (Al_i''') or a different type of co-ordination other than 6-fold (octahedral) or 4-fold (tetrahedral) can lead to a broadening of the diffraction line intensity. A few reports using nuclear magnetic resonance (NMR) spectroscopy provide some important information about the unnatural local chemical bonding in amorphous alumina specimens. Dupree *et al.*[42] showed using magic angle spinning (MAS)–NMR that 5-fold co-ordinated Al-O bonds (with a frequency of occurrence of almost 30%) exist in anodically formed amorphous alumina films. Two more recent papers[43,44] in which the authors report primarily 4-fold coordinated Al-O ($\sim$55%) and a significant fraction ($\sim$35%) of 5-fold co-ordinated Al-O in sputtered alumina thin films support this view conclusively. The percentage of, "amorphousness" is proportional to the fraction of 5-fold co-ordination. Such 5-fold co-ordination cannot happen in crystalline alumina but can be possible in a system that is transitioning to the crystallized state from amorphous. The non-stoichiometric composition and

the high energies in the plasma can freeze the sputtered ions into a metastable state between a crystal and purely disordered amorphous state.

The XPS results also support the hypothesis that the local electronic states are altered during the *a-γ* transition. In an ideal alumina structure, purely ionic bonding would lead to a conduction band (CB) that arises from Al anti-bonding orbitals which are empty (from the Al^{3+} ion) and the top of the VB would arise from the O 2p anti-bonding orbitals which are full (from the O^{2-} ions). Intuitively, the VB spectrum for a purely ionic solid must be dominated by energy levels of the anions. But the partial covalency of the atomic orbitals in real Al_2O_3 ensures the presence of Al-O bonding states below the VB edge, which can be presumed to control the distribution of the top of the VB. On a local scale, tetrahedral co-ordination (as in the case of *γ*-, *a*-Al_2O_3, Al-rich Al_2O_3) is associated with a more covalent character than octahedral co-ordination (α-Al_2O_3) due to the sp^3 hybridized orbitals. Such reorganizations in the VB can be evidenced from chemical state plots (Wagner plots) constructed from the photo and Auger electron spectral peaks. Fig. 10 shows the O1s-O KVV Wagner plot for the specimens used in this work and also standard values for bulk *γ* and α-Al_2O_3. There is only a minor positive shift in the modified Auger parameter (α′), i.e., screening effects of standard *γ* and α-Al_2O_3. Their positions in the Wagner plot are rationalized, since the octahedral coordination in α is associated with a higher initial state electron density and hence can be expected to increase the screening effect leading to a lower final state ion energy. However, a distinct demarcation is evident in the final ion energies in stable/metastable bulk oxides (BO) and in ultrathin thermally grown oxides (TGO), shown by the two shaded regions in the Wagner plot. The TGO are characterized by higher final state ion energies than bulk oxides. While the as deposited film lies in the region of BO, all the annealed specimens lie in the TGO regime. It is worth mentioning at this point that the interpretation of the Wagner plot based on the position of data points *along lines of constant α′* (slope = +1) is prone to effects of charging, while changes in absolute values of α′ (shifts normal to the diagonal with slope = −1) are more representative of the chemical state of the ions.[22,45] Hence, an intuitive difference can be inferred only in the annealed films: the 350 °C, 550 °C, and 750 °C annealed films show a slightly decreasing α′ trend, implying that the screening is reduced, probably by Al enrichment. Yet, all the data points cluster around an α′ value of 1039. Probably the theoretical models assume trivalent cations in a perfect lattice, while in actuality, the Al cations can have single, double, or triple charges and can be present in quasi octahedral or quasi tetrahedral co-ordinations too, particularly during the initial stages of growth or during the *a-γ* transition. Such abnormal co-ordination is not unfavourable when the surface energy is very low (which is the case in many of the transient aluminas like *γ* and *θ*) and most of the atoms lie on the surface of the crystal.[6,46]

It is also clear from our experimental observations that even at temperatures as low as 350 °C, sputtered amorphous alumina films are unstable against crystallization and nucleation can occur in the microstructure. In sputtered films,
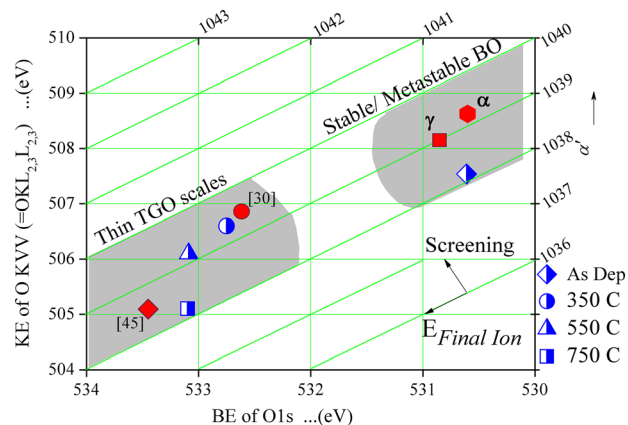

FIG. 10. A chemical state plot (Wagner plot) constructed from the oxygen photo electron and Auger electron peaks.

interdiffusion seems to precede product phase formation. However, the growth of the nuclei is severely curtailed, as the diffusion kinetics is too low at these temperatures to promote long range diffusion. Instead, as the frequency of the nuclei increase with temperature, crystallization progresses by coalescence of adjacent nuclei, as is evident from the images described above. The nucleation is also favoured by the energetics of the condensing ionic species, as is the case in sputtered films that condense from the plasma. Such mechanisms of cluster formation by coalescence have been reported by Chou and Nieh[47] in rf reactively sputtered alumina thin films, which lead to a layered structure formation. In Ref. 47, a similar amorphous/metastable *γ* mixture was found in the microstructure of the as deposited films. After annealing in the range of 800 °C to 1200 °C, there was strong evidence of texturing along the {400} and {440} planes and oriented growth in the perpendicular [001] direction as they detected from the nature of the electron diffraction spots. However, their samples were *plan-view* specimens prepared by direct deposition on Ni grids and in comparison with our results on *cross-sectioned* specimens—as seen by the two strong diffraction maxima consistently observed at 0.14 nm and 0.19 nm—it seems that there is a general tendency for the {400} and {440} *γ* planes to coalesce, irrespective of the substrate orientation or growth direction. The defect (vacancies in the Al sub-lattice) cubic spinel structure of the *γ*-Al_2O_3 is quite conducive for coalescence leading to a layered structure. The consistent appearance of rings in reciprocal space corresponding to $d_{hkl} = 0.199$ nm and 0.142 nm agree with this.

V. CONCLUSIONS

In summary, reactive magnetron sputtered amorphous alumina thin films have been annealed and characterized. The interface of the film with Si is Al-rich which develops into a thick interfacial reaction zone on annealing. The annealing process induces the *a-γ* transition characterized by the following features: Sharp rings at 0.19 nm and 0.142 nm in the TEM diffraction pattern; a diffraction halo with an outer maximal radius of ≈0.23 nm and a redistribution of the Al atoms from chemisorbed sites to tetrahedral and octahedral sites. The crystallization sequence seems to involve the

movement of cations to optimally coordinated sites. While the nucleation from the amorphous phase occurs by short range structural re-ordering, growth proceeds by clustering along favourable planes of adjacent nuclei. These processes involve changes in the local structure and also electronic state of the ions. Recent reports on ultra-thin a-Al$_2$O$_3$ films using EELS and XPS also point to a mechanism of local atomic rearrangement induced morphological transitions in a-Al$_2$O$_3$.[48] Similar mechanisms seem to be dominant in plasma deposited thin films too, as evident from the present study.

ACKNOWLEDGMENTS

[1]A. H. Carim, G. S. Rohrer, N. R. Dando, S-Y Tzeng, C. L. Rohrer, and A. J. Perrotta, J. Am. Ceram. Soc. **80**, 2677 (1997).

[2]I. Levin and D. G. Brandon, Philos. Mag. Lett. **77**, 117 (1998).

[3]G. W. Brindley and M. Nakahira, Nature **183**, 1620 (1959).

[4]K. N. Rao and H. Phil Ha, Catal. Sci. Technol. **2**, 495 (2012).

[5]N. Lock, M. Christensen, M. Ø. Jensen, and B. B. Iversen, Angew. Chem., Int. Ed. **50**, 7045 (2011).

[6]J. M. McHale, A. Auroux, A. J. Perrotta, and A. Navrotsky, Science **277**, 788 (1997).

[7]H. Knozinger and P. Ratnasamy, Catal. Rev.: Sci. Eng. **17**(1), 31 (1978).

[8]M. Ishida, I. Katakabe, and T. Nakamura, Appl. Phys. Lett. **52**, 1326 (1988).

[9]H. Wado, T. Shimizu, and M. Ishida, Appl. Phys. Lett. **67**, 2200 (1995).

[10]A. Stierle, F. Renner, R. Streitel, H. Dosch, W. Drube, and B. C. Cowie, Science **303**(5664), 1652 (2004).

[11]T. C. Chou and T. G. Nieh, Thin Solid Films **221**, 89 (1992).

[12]H. Momida, T. Hamada, Y. Takagi, T. Yamamoto, T. Uda, and T. Ohno, Phys. Rev. B **73**, 054108 (2006).

[13]C. M. Tanner, Y.-C. Perng, C. Frewin, S. E. Saddow, and J. P. Chang, Appl. Phys. Lett. **91**, 203510 (2007).

[14]X. Jiang, H. Oveisi, Y. Nemoto, N. Suzuki, K. C.-W. Wu, and Y. Yamauchi, Dalton Trans. **40**, 10851 (2011).

[15]T. W. Simpson, Q. Wen, N. Yu, and D. R. Clarke, J. Am. Ceram. Soc. **81**(1), 61 (1998).

[16]T. Nabatame, T. Yasuda, M. Nishizawa, M. Ikeda, T. Horikawa, and A. Toriyumi, Jpn. J. Appl. Phys., Part 1 **42**, 7205 (2003).

[17]T. M. Klein, D. Niu, W. S. Epling, W. Li, D. M. Maher, C. C. Hobbs, R. I. Hegde, I. J. R. Baumvol, and G. N. Parsons, Appl. Phys. Lett. **75**, 4001 (1999).

[18]P. Eklund, M. Sridharan, G. Singh, and J. Bøttiger, Plasma Process. Polym. **6**, S907 (2009).

[19]R. Methaapanon, S. M. Geyer, S. Brennan, and S. F. Bent, Chem. Mater. **25**, 3458 (2013).

[20]B. Chakraborty, S. Holloway, and J. K. Norskov, Surf. Sci. **152–153**, 660 (1985).

[21]R. van den Boomgaard and R. van Balen, CVGIP: Graphical Models and Image Processing **54**, 252 (1992).

[22]R. Bicker, H. Deger, W. Herzog, K. Rieser, H. Pulm, G. Hohlneicher, and H. J. Freund, J. Catal. **94**, 69 (1985).

[23]A. Mulligan, V. Dhanak, and M. Kadodwala, Langmuir **21**, 8312 (2005).

[24]A. Bianconi, R. Z. Bachrach, S. B. M. Hagstrom, and S. A. Flodstrom, Phys. Rev. B **19**, 2837 (1979).

[25]A. F. Carley and M. W. Roberts, Proc. R. Soc. London, Ser. A **363**, 403 (1978).

[26]G. Lefevre, M. Duc, P. Lepeut, R. Caplain, and M. Fedoroff, Langmuir **18**, 7530 (2002).

[27]M. Yoshitake, W. Song, J. Libra, K. Masek, F. Sutara, V. Matolin, and K. C. Prince, J. Appl. Phys. **103**, 033707 (2008).

[28]M. Yoshitake, W. Song, J. Libra, K. Masek, F. Sutara, V. Matolin, and K. C. Prince, Appl. Surf. Sci. **256**, 3051 (2010).

[29]M. Yoshitake, S. Nemsak, T. Skala, N. Tsud, T. Kim, V. Matolin, and K. C. Prince, Surf. Sci. **604**, 2150 (2010).

[30]C. D. Wagner, D. E. Passoja, H. F. Hillery, T. G. Kinisky, H. A. Six, W. T. Jansen, and J. A. Taylor, J. Vac. Sci. Technol. **21**, 933 (1982).

[31]T. L. Baar, Appl. Surf. Sci. **15**, 1 (1983).

[32]H. J. Kim, S. Yong No, D. Eom, and C. S. Hwang, J. Korean. Phys. Soc. **49**, 1271 (2006).

[33]J. A. Rotole and P. M. A. Sherwood, J. Vac. Sci. Technol. **17**, 1091 (1999).

[34]Y. Li, S. Zhang, Y. Liu, T. P. Chen, T. Sritharan, and C. Xu, J. Nanosci. Nanotechnol. **9**, 4116 (2009).

[35]Y. Liu, S. Zhang, T. P. Chen, X. B. Chen, W. Zhu, S. Fung, M. Yang, Z. H. Cen, J. I. Wong, and Y. B. Li, Appl. Phys. Lett. **93**, 142106 (2008).

[36]K. Sohlberg, S. J. Pennycook, and S. T. Pantelides, J. Am. Chem. Soc. **121**, 7493 (1999).

[37]X. Krokidis, P. Raybaud, A.-E. Gobichon, B. Rebours, P. Euzen, and H. Toulhoat, J. Phys. Chem. B **105**, 5121 (2001).

[38]R.-S. Zhou and R. L. Snyder, Acta Cryst. B **47**, 617 (1991).

[39]G. Gutierrez, A. Taga, and B. Johansson, Phys. Rev. B **65**, 012101 (2001).

[40]P. Bai, P. Wu, Z. Yan, and X. S. Zhao, J. Mater. Chem. **19**, 1554 (2009).

[41]W. Engelhart, W. Dreher, O. Eibl, and V. Schier, Acta Mater. **59**, 7757 (2011).

[42]R. Dupree, I. Farnan, A. J. Forty, S. El-Mashiri, and L. Bottyan, J. Phys. Colloques **46**, C8–113 (1985).

[43]S.-K. Lee, S.-Y. Park, Y.-S. Yi, and J. Moon, J. Phys. Chem. C **114**, 13980 (2010).

[44]S.-K. Lee, S. Bo Lee, S. Y. Park, Y.-S. Yi, and C. W. Ahn, Phys. Rev. Lett. **103**, 095501 (2009).

[45]P. C. Snijders, L. P. H. Jeurgens, and W. G. Sloof, Surf. Sci. **589**, 98 (2005).

[46]Z. Lodziana, N.-Y. Topsoe, and J. K. Norskov, Nature Mater. **3**, 289 (2004).

[47]T. C. Chou and T. G. Nieh, J. Am. Ceram. Soc. **74**, 2270 (1991).

[48]L. Bloch, Y. Kauffmann, and B. Pokroy, Cryst. Growth Des. **14**, 3983 (2014).